Residual Stress and Opening-Mode Fracture Analysis of Multilayered Structures Subjected to Thermal Loading

Xin He, Ph.D.[1]; Ross Larsen, Ph.D.[2]; Fangliang Chen, Ph.D.[3]; and Huiming Yin, Ph.D., M.ASCE[4]

Abstract: Temperature change after formation commonly results in thermal residual stress in multilayered structures due to the different thermal and mechanical properties of each layer. In this paper, a three-dimensional (3D) elastic model is developed to study the residual stress and opening-mode fractures (OMFs) in a multilayered structure consisting of arbitrary number of layers under temperature change. The general solution of displacement field in the multilayered structure is derived by solving the elastic boundary value problem. In order to verify the proposed model, the elastic field in the advanced polymeric solar reflectors that consist of four layers is solved by applying the present model and compared with the finite-element (FE) simulation. In addition, parametric studies are conducted to investigate the effect of the thickness ratio between each layer on the accuracy of the developed model. Based on the obtained elastic field, the fracture energy release rate (ERR) in the surface layer of the advanced polymeric reflector is obtained and used to study the fracture initiation, infilling, and saturation successfully. **DOI: 10.1061/(ASCE)EM.1943-7889.0001579.** *© 2019 American Society of Civil Engineers.*

Downloaded from ascelibrary.org by Columbia University on 06/11/19. Copyright ASCE. For personal use only; all rights reserved.

Introduction

Multilayered materials or structures have been widely used in advanced material design, such as multilayered advanced polymeric solar reflectors (Kennedy et al. 2005; Jorgensen et al. 2010; Sutter et al. 2012; Zhang et al. 2016, 2017; Sansom et al. 2016), surface protective coatings (Çolak 2001; Yin et al. 2007c), thin film/substrate systems (Beuth 1992; Xia and Hutchinson 2000; Freund and Suresh 2004; Yin et al. 2008; Chen et al. 2015; He et al. 2017), and pavements (Timm et al. 2003; Yin 2010b; Yin et al. 2007a). Due to their advanced mechanical and thermal properties, the brittle metal oxide thin films are typically coated as the surface layer in the multilayered structures for protective purposes. When subjected to a thermal loading, residual stress would be introduced in the multilayered structures due to the material mismatch, particularly the large difference of thermal expansion coefficients. Once the thermal loading reaches the critical value, the multilayered structure is prone to premature failure because of opening-mode fractures (OMFs) in the brittle surface coating, driven by the developed residual stress (Ochiai et al. 2005; Roy and Ghosh 2016). As a result, the cracking would affect the performance and structure integrity of the devices and eventually jeopardize their functions. Therefore, it is essential to understand the residual stresses and their resulting fracture mechanisms in multilayered structures in order to preserve their capabilities under typical levels of thermally induced residual stress.

Initially, studies about the cracking behaviors of multilayered structures have focused on the local elastic solutions in the neighborhood of the singular point that exists at the crack tip, which is located at the interface between the fractured and intact layers (Beuth 1992; Xia and Hutchinson 2000; Suo and Hutchinson 1989; Ye et al. 1992; Beuth and Klingbeil 1996; Li and Chou 1997; Hsueh and Yanaka 2003; Wellner et al. 2004; Thouless et al. 2011; Chai 2011; Chai and Fox 2012). Although such local solutions are useful in the study of fracture propagation, they cannot be directly used to predict fracture initiation, fracture spacing, or to study the interaction between fractures (Yin 2010b). According to the studies of Bai and his coworkers (Bai et al. 2000a, b; Bai and Pollard 2000), an overall elastic field in the thin film that is based on the complete set of governing equations for the elastic boundary value problems should be used to completely understand fracture spacing. Later, Yin and his coworkers proposed a plane-strain elastic model (Yin et al. 2008; Yin 2010a, b; Yin and Prieto-Muñoz 2013), where the closed-form elastic solutions in the coating/substrate structure were obtained and used to interpret fracture initiation, infilling, and saturation caused by tension in the layered materials successfully.

For the case where thermal loading is applied to the multilayered structures, cracks along both the longitudinal and transverse directions would present in the surface coating because the thermal loading introduces biaxial residual stress in the structures. In this case, neither the plane stress nor plane strain assumption can be applied and a full three-dimensional (3D) residual stress analysis is required. According the literature, the residual stress in multilayered structures is primarily obtained based on experimental measurements or numerical simulations (Stoney 1909; Berry 1989; Ohring 2001; Schwarzer and Richter 2006; Ochiai et al. 2005), while very few theoretical models can be found (Evans and Hutchinson 1995; Hutchinson 1996; Hsueh and Yanaka 2003; Zhang et al. 2007; Ahmed et al. 2011; Roy and Ghosh 2016). The details about these testing methods and theoretical models are summarized as follows.

[1]Research Scientist, Computational Science Center, National Renewable Energy Laboratory, 15013 Denver W. Pkwy., Golden, CO 80401 (corresponding author). Email: xh2205@columbia.edu

[2]Senior Scientist, Computational Science Center, National Renewable Energy Laboratory, 15013 Denver W. Pkwy., Golden, CO 80401.

[3]Associate Research Scientist, Dept. of Civil Engineering and Engineering Mechanics, Columbia Univ., 610 Seeley W. Mudd 500 West 120th St., New York, NY 10027.

[4]Associate Professor, Dept. of Civil Engineering and Engineering Mechanics, Columbia Univ., 610 Seeley W. Mudd 500 West 120th St., New York, NY 10027.

Note. This manuscript was submitted on April 9, 2018; approved on September 4, 2018; published online on January 14, 2019. Discussion period open until June 14, 2019; separate discussions must be submitted for individual papers. This paper is part of the ***Journal of Engineering Mechanics***, © ASCE, ISSN 0733-9399.

In 1909, Stoney (1909) proposed a formula to predict the residual stress in thin film/substrate systems based on the curvature of the elastically deformed coated substrate

$$\sigma_{zz}^{f} \approx -E_s \frac{h_s^2}{6h_f R} \tag{1}$$

where E_s = Young's modulus of substrate; R = radius of curvature; h_s = thickness of substrate; and h_f = thickness of coating. The index zz denotes the stress component in direction of the length side of the beam. Later, Berry (1989) observed that the substrate curls into an approximately cylindrical shape instead of showing a bowl or cap-like deformation and argued that the plate modulus should be used to replace E_s. Based on the measurement of a thin films deposited on a platelike substrate, Ohring (2001) argued that the corresponding biaxial deformation has to be taken into account by using the biaxial modulus. After examined different forms of Stoney's equation by applying a correct 3D finite-element (FE) model, Schwarzer and Richter (2006) found the biaxial modulus would yield an accurate result while the plate modulus would deliver a bigger stress by 20%–30%. Stoney's equation uses the results from experimental measurement and predict a uniformly distributed normal stress in the coating. Ochiai et al. (2005) summarized an equation to predict the residual stress in coating/substrate system based on the applied thermal loading or tensile stress by fitting the experimental data, then the crack spacing of the coating was studied by employing a strength criteria. However, this equation is only valid for that specific material combination and geometry design.

Theoretical models have been developed to predict the residual stress in multilayered structures under thermal loading. Evans and Hutchinson (1995) presented several models to study the mechanisms that rise to tensile stresses in thin film deposition, and gave the expression of residual stress in a thin film that is attached to an infinite substrate. Later, a form of residual stress in the thin coating bonded to a substrate that is allowed to expand or shrink freely was proposed by Hutchinson (1996) based on the assumption that the substrate is effectively uninfluenced by the film and the substrate imposes its in-plane strains on the film. This model assumed that the shear strain in the film is equal to that in substrate away from the edges, so it can be used to predict the stress in the center area; however, more accurate displacement and stress distributions at the edge are required for cracking analysis. Another closed-form analytical solution to predict the stress distribution in a film segment when the film/substrate system was subjected to both residual stresses and tensile loading was derived by Hsueh and Yanaka (2003) in 2003, including the effects of external loading into the shear lag model. Also, the cracking in coating was predicted by adopting both strength and energy criteria based on the solved stress and displacement. However, only the normal stress along the same direction as the external loading was considered in this model, which would introduce significant error when the thermal loading is comparable with the external loading. Based on the force and moment balances, Zhang et al. (2007) proposed another analytical model to predict the thermal residual stress in multilayered coating systems. In this model, the total strains of the coating layer and the substrate were decomposed into an in-plane strain and a bending strain; following this a closed-form solution of thermal stresses was obtained, which possesses the merit of independence of the number of coating layers. In 2011, Ahmed et al. (2011) developed a new shear lag model by considering the effect of the substrate plasticity based on a study by Hsueh and Yanaka (2003) to evaluate the residual stress in a diamond coating as a function of the strain applied to the ductile substrate. The theoretical solutions were then verified by experimental data measured using the micro-Raman spectroscopy. Recently, Roy and Ghosh (2016) proposed another model to predict the residual stress in the free expanded galvannealed coating/substrate structure using the method of superposition. The normal stress in both coating and substrate were obtained. Based on the residual stress, the fracture energy release rate (ERR) in the coating along both longitudinal and transversal directions were obtained and used to predict the crack spacing. The experimental verification showed that the predicted crack spacings were quite different from the observed results and the proposed model underestimated the crack spacing by more than a factor of two. The drawback of this proposed model is that the solved normal strains in coating are constant and depend on the material properties only. Therefore, this model cannot capture the strain and stress distribution accurately enough to predict crack formation.

It is clear that the residual stress in the multilayered stress should depend on the material properties and geometric constants of *each* layer, therefore none of the literature approaches mentioned previously can predict the residual stress in multilayered structures accurately. To fulfill this gap, we propose in this paper another 3D elastic model to predict the residual stress in multilayered structures considering the effect of material mismatch and layer thicknesses. The solved residual stress from this model can be used to conduct the fracture analysis based on either energy or strength model.

Consider a multilayered structure consisting of N layers. All layers are fully bonded together such that there is no debonding or slipping between layers and the displacements at all interfaces must be continuous. The Young's modulus, Poisson ratio, and the thermal expansion coefficient for each layer are denoted by E^i, ν_i, and α_i, respectively, where the subscript and superscript $i = 1, 2, \ldots, N$ represents the ith layer. The thickness of the ith layer is h_i, and the z-coordinate of the lower surface of the ith layer is t_{i-1} while it is t_i for the upper surface of layer i. The total thickness of the multilayered structure is h. The boundary conditions are set such that the displacement along the thickness direction at the bottom is fixed but it is free to expand along the length and width directions. Once the temperature change reaches the critical value, OMFs would initiate in the brittle surface layer and propagate toward the interface. To simplify our analysis, the length and width of the model are set to be coincident and equal to 2λ as the structure would be cracked into square pieces eventually if the temperature change is high enough. It would be straightforward to generalize our approach to include nonsquare sample shapes. Considering a section between four adjacent OMFs, a simplified model is built and shown Fig. 1.

The remainder of this paper is organized as follows. The section "Formulations for 3D Elastic Field Analysis" will formulate the problem and provide an explicit solution of the 3D elastic field in the multilayered structure. The approach leads to the solutions that are solved from the bottom of the stack to the top, with the solution in the first layer being used to construct the solution in the second layer and so on, up to the top of the stack. Section "Numerical Verification of the General Solutions" will study the distribution of residual stress and displacement in a multilayered stack representative of an advanced polymeric solar reflector, based on the developed formulations in the section "Formulations for 3D Elastic Field Analysis." Parametric studies also are included in the section "Numerical Verification of the General Solutions" to investigate the applicability of the proposed model to structures with layers of different thicknesses by comparing the theoretical predictions with FE analysis results. The calculation of fracture ERR based on the obtained elastic field and some discussions about the fracture analysis are presented in section "Fracture Analysis." Finally, some discussion and conclusions are presented in section "Summary and Conclusions."

Downloaded from ascelibrary.org by Columbia University on 06/11/19. Copyright ASCE. For personal use only; all rights reserved.

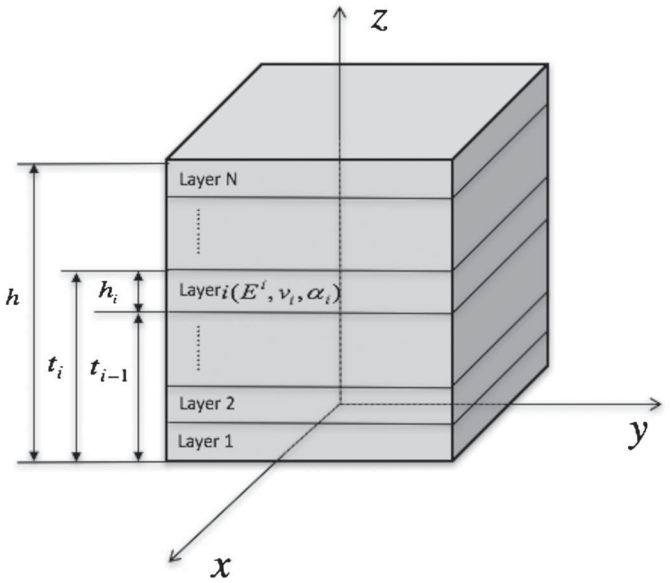

Fig. 1. Schematic illustration of the multilayered structure with N different material layers.

Formulations for 3D Elastic Field Analysis

Applying the small displacement assumption, the residual stress, caused by a temperature change of ΔT, in the multilayered structures can be written as

$$\sigma_{xx}^i = \frac{E^i}{(1+\nu_i)(1-2\nu_i)}[(1-\nu_i)u_{x,x}^i + \nu_i u_{y,y}^i + \nu_i u_{z,z}^i] - \frac{\Delta T \alpha_i E^i}{1-2\nu_i} \tag{2}$$

$$\sigma_{yy}^i = \frac{E^i}{(1+\nu_i)(1-2\nu_i)}[(1-\nu_i)u_{y,y}^i + \nu_i u_{x,x}^i + \nu_i u_{z,z}^i] - \frac{\Delta T \alpha_i E^i}{1-2\nu_i} \tag{3}$$

$$\sigma_{zz}^i = \frac{E^i}{(1+\nu_i)(1-2\nu_i)}[(1-\nu_i)u_{z,z}^i + \nu_i u_{x,x}^i + \nu_i u_{y,y}^i] - \frac{\Delta T \alpha_i E^i}{1-2\nu_i} \tag{4}$$

$$\tau_{xy}^i = \frac{E^i(u_{x,y}^i + u_{y,x}^i)}{2(1+\nu_i)} \tag{5}$$

$$\tau_{xz}^i = \frac{E^i(u_{x,z}^i + u_{z,x}^i)}{2(1+\nu_i)} \tag{6}$$

$$\tau_{yz}^i = \frac{E^i(u_{y,z}^i + u_{z,y}^i)}{2(1+\nu_i)} \tag{7}$$

where u_x^i, u_y^i, and u_z^i are the displacements along x-direction, y-direction, and z-direction in the ith layer respectively.

Substituting the stress into the equilibrium equations yields

$$\frac{2(1-\nu_i)}{1-2\nu_i}u_{x,xx}^i + u_{x,yy}^i + u_{x,zz}^i + \frac{1}{1-2\nu_i}(u_{y,xy}^i + u_{z,xz}^i) = 0 \tag{8}$$

$$\frac{2(1-\nu_i)}{1-2\nu_i}u_{y,yy}^i + u_{y,xx}^i + u_{y,zz}^i + \frac{1}{1-2\nu_i}(u_{x,xy}^i + u_{z,yz}^i) = 0 \tag{9}$$

Although the multilayered structure is fixed along the thickness direction at the bottom, the material mismatch has only minor effect on the displacement and normal stress along the thickness direction so it is reasonable to assume the normal stress along the z-direction is zero (Ochiai et al. 2005)

$$\sigma_{zz}^i = 0 \tag{10}$$

Combining Eqs. (4) and (10), the normal strain in z-direction ($u_{z,z}^i$) can be written as a function of the strain along x- and y-directions

$$u_{z,z}^i = \frac{1+v_i}{1-v_i}\Delta T \alpha_i - \frac{v_i}{1-v_i}(u_{x,x}^i + u_{y,y}^i) \tag{11}$$

In addition, we assume that all lines which were parallel to x or y-axis before deformation will stay parallel to the corresponding axis after deformation, indicating that every cross section perpendicular to z-axis will keep be square after deformation (nonshearing assumption). Mathematically, this assumption results in

$$u_{x,y}^i = u_{y,x}^i = 0 \tag{12}$$

Next, substitute Eqs. (11) and (12) into Eqs. (8) and (9), to simplify the equilibrium equations to

$$\frac{2-\nu^i}{1-\nu_i}u_{x,xx}^i + u_{x,zz}^i = 0 \tag{13}$$

and

$$\frac{2-\nu^i}{1-\nu_i}u_{y,yy}^i + u_{y,zz}^i = 0 \tag{14}$$

General Solution of the Displacement in x-Direction

Eq. (13) is a decoupled partial differential equation of u_x^i. By applying the method of separation of variables, the general solution of u_x^i can be written as

$$u_x^i = f(x)g(z) + \varepsilon_u x \tag{15}$$

where $f(x)$ is a function of x; $g(z)$ is a function of z; and ε_u is used to account for the uniform strain.

Substituting Eq. (15) into Eq. (13) produces

$$\frac{2-\nu_i}{1-\nu_i}\frac{f''}{f} + \frac{g''}{g} = 0 \tag{16}$$

and because f and f'' are functions of x while g and g'' are functions of z, these two terms in Eq. (16) can be linked by an independent constant C^2

$$\frac{f''}{f} = -\frac{1-\nu_i}{2-\nu_i}\frac{g''}{g} = C^2 \tag{17}$$

From Eq. (17), the general solution of u_x^i can be obtained

$$u_x^i = [a_1^i \sinh(Cx) + a_2^i \cosh(Cx)][a_3^i \sin(\xi_i Cz) + a_4^i \cos(\xi_i Cz)] + \varepsilon_u x \tag{18}$$

where

$$\xi_i = \sqrt{\frac{2-\nu_i}{1-\nu_i}} \tag{19}$$

and a_1^i, a_2^i, a_3^i, and a_4^i are constants to be determined.

J. Eng. Mech., 2019, 145(3): 04019010

Downloaded from ascelibrary.org by Columbia University on 06/11/19. Copyright ASCE. For personal use only; all rights reserved.

The symmetry of u_x^i at $x = 0$ implies that

$$u_x^i(x = 0) = 0 \tag{20}$$

and applying Eq. (20) into Eq. (18) yields $a_2^i = 0$ and the general solution of u_x^i reduces to be

$$u_x^i = \sinh(Cx)[A_i \sin(\xi_i Cz) + B_i \cos(\xi_i Cz)] + \varepsilon_u x \tag{21}$$

where A_i and B_i are unknowns to be determined for each layer.

As stated before, the material mismatch has minor effect on the displacement along the z-direction, and u_z^i is primarily controlled by the thermal expansion and Poisson ratio's effect, therefore $u_{z,x}^i << u_{x,z}^i$. Hence, we will ignore the contribution of $u_{z,x}^i$ to the shearing stress of τ_{xz}^i in the rest of our treatment. With this approximation, the shearing stress τ_{xz}^i can be reduced to be

$$\tau_{xz}^i = \frac{E^i \xi_i C}{2(1+\nu_i)} \sinh(Cx)[A_i \cos(\xi_i Cz) - B_i \sin(\xi_i Cz)] \tag{22}$$

Displacement in Layer 1

For Layer 1, the general solution of u_x^1 and τ_{xz}^1 can be written as

$$u_x^1 = \sinh(Cx)[A_1 \sin(\xi_1 Cz) + B_1 \cos(\xi_1 Cz)] + \varepsilon_u x \tag{23}$$

and

$$\tau_{xz}^1 = \frac{E^1 \xi_1 C}{2(1+\nu_1)} \sinh(Cx)[A_1 \cos(\xi_1 Cz) - B_1 \sin(\xi_1 Cz)] \tag{24}$$

The zero shearing stress boundary condition at the bottom, $\tau_{xz}^1(z = 0) = 0$, gives $A_1 = 0$. Then Eqs. (23) and (24) reduce to

$$u_x^1 = B_1 \sinh(Cx) \cos(\xi_1 Cz) + \varepsilon_u x \tag{25}$$

and

$$\tau_{xz}^1 = \frac{-B_1 E^1 \xi_1 C}{2(1+\nu_1)} \sinh(Cx) \sin(\xi_1 Cz) \tag{26}$$

where B_1, C, and ε_u are unknowns to be determined using the boundary conditions.

With the symmetry used previously, Eq. (25) has a simpler form than Eq. (23), but it will be useful to keep the more general form for purposes of relating the Layer 1 equations to the equations in the upper layers, so we introduce two parameters

$$H_{11} = 0 \tag{27}$$

and

$$H_{12} = 1 \tag{28}$$

so that

$$u_x^1 = B_1 \sinh(Cx)[H_{11} \sin(\xi_1 Cz) + H_{12} \cos(\xi_1 Cz)] + \varepsilon_u x \tag{29}$$

and

$$\tau_{xz}^1 = \frac{B_1 E^1 \xi_1 C}{2(1+\nu_1)} \sinh(Cx)[H_{11} \cos(\xi_1 Cz) - H_{12} \sin(\xi_1 Cz)] \tag{30}$$

The notation is defined so that the first index for each $H_{n(1,2)}$ indicates the layer number, and the second index (1 or 2) indicates whether the H multiplies a cosine or a sine function in the displacement equation.

Displacement in Layer 2

Eqs. (21) and (22) give the general solution of u_x^2 and τ_{xz}^2

$$u_x^2 = \sinh(Cx)[A_2 \sin(\xi_2 Cz) + B_2 \cos(\xi_2 Cz)] + \varepsilon_u x \tag{31}$$

and

$$\tau_{xz}^2 = \frac{E^2 \xi_2 C}{2(1+\nu_2)} \sinh(Cx)[A_2 \cos(\xi_2 Cz) - B_2 \sin(\xi_2 Cz)] \tag{32}$$

Because we assume there is no slipping between each layer, the in-plane displacements are continuous. In addition, according to Newton's third law, the stresses at the interface are also continuous. Specifically, the continuity of the displacement and shearing stress at the interface of Layers 1 and 2, $u_x^1(z = t_1) = u_x^2(z = t_1)$ and $\tau_{xz}^1(z = t_1) = \tau_{xz}^2(z = t_1)$, implies the following relationships:

$$\begin{aligned} &A_2 \sin(\xi_2 Ct_1) + B_2 \cos(\xi_2 Ct_1) \\ &\quad = B_1[H_{11} \sin(\xi_1 Ct_1) + H_{12} \cos(\xi_1 Ct_1)] \end{aligned} \tag{33}$$

$$\begin{aligned} &A_2 \cos(\xi_2 Ct_1) - B_2 \sin(\xi_2 Ct_1) \\ &\quad = \frac{B_1 E^1 \xi_1 (1+\nu_2)}{E^2 \xi_2 (1+\nu_1)}[H_{11} \cos(\xi_1 Ct_1) - H_{12} \sin(\xi_1 Ct_1)] \end{aligned} \tag{34}$$

Based on Eqs. (33) and (34), the unknowns in Layer 2, A_2 and B_2, are solved in terms of B_1 as

$$A_2 = H_{21} B_1 \tag{35}$$

and

$$B_2 = H_{22} B_1 \tag{36}$$

where

$$\begin{aligned} H_{21} = {} & [H_{11} \sin(\xi_1 Ct_1) + H_{12} \cos(\xi_1 Ct_1)] \sin(\xi_2 Ct_1) \\ & + \frac{E^1 \xi_1 (1+\nu_2)}{E^2 \xi_2 (1+\nu_1)}[H_{11} \cos(\xi_1 Ct_1) \\ & - H_{12} \sin(\xi_1 Ct_1)] \cos(\xi_2 Ct_1) \end{aligned} \tag{37}$$

and

$$\begin{aligned} H_{22} = {} & [H_{11} \sin(\xi_1 Ct_1) + H_{12} \cos(\xi_1 Ct_1)] \cos(\xi_2 Ct_1) \\ & - \frac{E^1 \xi_1 (1+\nu_2)}{E^2 \xi_2 (1+\nu_1)}[H_{11} \cos(\xi_1 Ct_1) \\ & - H_{12} \sin(\xi_1 Ct_1)] \sin(\xi_2 Ct_1) \end{aligned} \tag{38}$$

Displacement in Layer i ($2 < i < N$)

Repeating the same procedures as in section "Displacement in Layer 2," for Layer $3, 4, \ldots, N-1$, the displacement and shearing stress for layer i can be summarized as

$$u_x^i = B_1 \sinh(Cx)[H_{i1} \sin(\xi_i Cz) + H_{i2} \cos(\xi_i Cz)] + \varepsilon_u x \tag{39}$$

and

$$\tau_{xz}^i = \frac{B_1 E^i \xi_i C}{2(1+\nu_i)} \sinh(Cx)[H_{i1} \cos(\xi_i Cz) - H_{i2} \sin(\xi_i Cz)] \tag{40}$$

where

Downloaded from ascelibrary.org by Columbia University on 06/11/19. Copyright ASCE. For personal use only; all rights reserved.

$$H_{i1} = [H_{(i-1)1}\sin(\xi_{i-1}Ct_{i-1}) + H_{(i-1)2}\cos(\xi_{i-1}Ct_{i-1})]\sin(\xi_i Ct_{i-1}) + \frac{E^{i-1}\xi_{i-1}(1+\nu_i)}{E^i\xi_i(1+\nu_{i-1})}[H_{(i-1)1}\cos(\xi_{i-1}Ct_{i-1}) - H_{(i-1)2}\sin(\xi_{i-1}Ct_{i-1})]\cos(\xi_i Ct_{i-1}) \quad (41)$$

$$H_{i2} = [H_{(i-1)1}\sin(\xi_{i-1}Ct_{i-1}) + H_{(i-1)2}\cos(\xi_{i-1}Ct_{i-1})]\cos(\xi_i Ct_{i-1}) - \frac{E^{i-1}\xi_{i-1}(1+\nu_i)}{E^i\xi_i(1+\nu_{i-1})}[H_{(i-1)1}\cos(\xi_{i-1}Ct_{i-1}) - H_{(i-1)2}\sin(\xi_{i-1}Ct_{i-1})]\sin(\xi_i Ct_{i-1}) \quad (42)$$

Displacement in Layer N

For the surface layer, the general solution of u_x^N and τ_{xz}^N can be written as

$$u_x^N = \sinh(Cx)[A_N\sin(\xi_N Cz) + B_N\cos(\xi_N Cz)] + \varepsilon_u x \quad (43)$$

and

$$\tau_{xz}^N = \frac{E^N\xi_N C}{2(1+\nu_N)}\sinh(Cx)[A_N\cos(\xi_N Cz) - B_N\sin(\xi_N Cz)] \quad (44)$$

Applying the free shearing stress boundary condition at the top surface, $\tau_{xz}^N(z=h)=0$, A_N and B_N are related by the following equation:

$$A_N\cos(\xi_N Ch) = B_N\sin(\xi_N Ch) \quad (45)$$

Therefore, Eqs. (43) and (44) are further simplified to

$$u_x^N = D_N\sinh(Cx)\cos(\xi_N Ch - \xi_N Cz) + \varepsilon_u x \quad (46)$$

and

$$\tau_{xz}^N = \frac{D_N E^N\xi_N C}{2(1+\nu_N)}\sinh(Cx)\sin(\xi_N Ch - \xi_N Cz) \quad (47)$$

where D_N is a constant to be determined.

General Solution of Displacement in y-Direction

For this special case where the length and width of the structure are coincident, the displacement in y-direction can be obtained in the same fashion. Therefore, by replacing x with y and y with x in u_x^i, the displacement and shearing stress along y-direction can be obtained. For Layer 1 to Layer $N-1$

$$u_y^i = B_1\sinh(Cy)[H_{i1}\sin(\xi_i Cz) + H_{i2}\cos(\xi_i Cz)] + \varepsilon_u y \quad (48)$$

and

$$\tau_{yz}^i = \frac{B_1 E^i\xi_i C}{2(1+\nu_i)}\sinh(Cy)[H_{i1}\cos(\xi_i Cz) - H_{i2}\sin(\xi_i Cz)] \quad (49)$$

For Layer N

$$u_y^N = D_N\sinh(Cy)\cos(\xi_N Ch - \xi_N Cz) + \varepsilon_u x \quad (50)$$

and

$$\tau_{yz}^N = \frac{D_N E^N\xi_N C}{2(1+\nu_N)}\sinh(Cy)\sin(\xi_N Ch - \xi_N Cz) \quad (51)$$

Eqs. (27), (28), (37), (38), (41), and (41) still hold for these equations as well.

General Solution of Displacement in z-Direction

Once u_x and u_y are solved for each layer, the general solution of u_z^i can be determined by integrating Eq. (11) along the z-direction for each layer. Note that the integration of Eq. (11) along z-direction would introduce an unknown function $F_i(x,y)$ for each layer. By applying the fixed boundary condition at the bottom $[u_z^1(z=0)=0]$ and the continuity of u_z at each interface, N equations are obtained, which can then used to solve the N unknown functions $F_i(x,y)$, $i=1,2,\ldots,N$. As this study focuses on the OMF analysis, the displacement and normal stress along z-direction is less interesting than the displacement and normal stresses along x- and y-directions, which are essential for the OMF analysis. Based on Eqs. (2) and (3), the normal stress σ_{xx}^i and σ_{yy}^i are functions of $u_{z,z}^i$, which can be obtained through Eq. (11) after solving u_x^i and u_y^i. Therefore, detailed derivation of displacement along z-direction, u_z^i, will not be presented in this paper.

General Solution of the Normal Stress

By inserting the solved displacement for each layer into Eq. (11), the strain along the z-direction, $u_{z,z}$ can be obtained. Substituting the resulting $u_{z,z}$, u_x, and u_y into Eqs. (2) and (3), the general solution of the in plane normal stress for Layers i, $i\in[1,N-1]$, can be determined as

$$\sigma_{xx}^i = \frac{E^i}{1-\nu_i^2}[B_1 C[H_{i1}\sin(\xi_i Cz) + H_{i2}\cos(\xi_i Cz)][\cosh(Cx) + \nu_i\cosh(Cy)] + (1+\nu_i)(\varepsilon_u - \Delta T\alpha_i)] \quad (52)$$

and

$$\sigma_{yy}^i = \frac{E^i}{1-\nu_i^2}[B_1 C[H_{i1}\sin(\xi_i Cz) + H_{i2}\cos(\xi_i Cz)] \times [\cosh(Cy) + \nu_i\cosh(Cx)] + (1+\nu_i)(\varepsilon_u - \Delta T\alpha_i)] \quad (53)$$

and the normal stress in the surface layer reads

$$\sigma_{xx}^N = \frac{E^N}{1-\nu_N^2}[B_N C\cos(\xi_N Ch - \xi_N Cz)[\cosh(Cx) + \nu_N\cosh(Cy)] + (1+\nu_N)(\varepsilon_u - \Delta T\alpha_N)] \quad (54)$$

$$\sigma_{yy}^N = \frac{E^N}{1-\nu_N^2}[B_N C\cos(\xi_N Ch - \xi_N Cz)[\cosh(Cy) + \nu_N\cosh(Cx)] + (1+\nu_N)(\varepsilon_u - \Delta T\alpha_N)] \quad (55)$$

Explicit Displacement Field

Until now, the general solution of the displacement field in the multilayered structures has been solved. However, there are still four unknowns (B_1, D_N, C, and ε_u) that need to be determined to completely specify the solution. In the following subsections, the continuity and boundary conditions are applied to determine these unknowns.

Continuity at the Interface

Consider the continuity of displacement and shearing stress at the interface between Layer $N-1$ and Layer N, $u_x^{N-1}(z=t_{N-1}) = u_x^N(z=t_{N-1})$ and $\tau_{xz}^{N-1}(z=t_{N-1}) = \tau_{xz}^N(z=t_{N-1})$, we have

$$D_N\cos(\xi_N Ch_N) = B_1[H_{(N-1)1}\sin(\xi_{N-1}Ct_{N-1}) + H_{(N-1)2}\cos(\xi_{N-1}Ct_{N-1})] \quad (56)$$

J. Eng. Mech., 2019, 145(3): 04019010

Downloaded from ascelibrary.org by Columbia University on 06/11/19. Copyright ASCE. For personal use only; all rights reserved.

and

$$D_N \sin(\xi_N C h_N) = \frac{B_1 E^{N-1} \xi_{N-1}(1+\nu_N)}{E^N \xi_N (1+\nu_{N-1})} [H_{(N-1)1} \cos(\xi_{N-1} C t_{N-1}) - H_{(N-1)2} \sin(\xi_{N-1} C t_{N-1})] \tag{57}$$

Combine Eqs. (56) and (57) by solving both for D_N and setting the results equal, so that a nonlinear equation in terms of C is obtained

$$[H_{(N-1)1} \sin(\xi_{N-1} C t_{N-1}) + H_{(N-1)2} \cos(\xi_{N-1} C t_{N-1})] \sin(\xi_N C h_N) = \frac{E^{N-1} \xi_{N-1}(1+\nu_N)}{E^N \xi_N (1+\nu_{N-1})} [H_{(N-1)1} \cos(\xi_{N-1} C t_{N-1}) - H_{(N-1)2} \sin(\xi_{N-1} C t_{N-1})] \cos(\xi_N C h_N) \tag{58}$$

As $H_{(N-1)1}$, $H_{(N-1)2}$, H_{N1}, and H_{N1} are functions of material properties and geometric constants, therefore the only unknown in Eq. (58) is C. By solving this nonlinear equation numerically, the unknown C, which is a function of material properties and thickness but independent of the length and width, can be determined. According to Yin and Prieto-Muñoz (2013), many solutions exist for constant C because of the periodicity of the sin() and cos() functions, which suggests the need for a series-form solution. In general, the roots of C in Eq. (58) are not periodic, which implies that the basis functions in the series-form solution are not orthonormal to each other. Therefore, the derivation of the coefficient of each basis function will be complicated and the convergence of the solution will still be open. For simplicity, this study chooses the first root to demonstrate this theory.

Free Normal Stress at the Side Faces

After solving C, there are three unknowns left, B_1, D_N, and ε_u, which require three more boundary conditions to be determined. As the combination of Eqs. (56) and (57) is used to solve C, therefore either Eq. (56) or Eq. (57) can be further used to determine other unknowns. Based on this fact, two more boundary conditions are sufficient in order to get the explicit elastic solution.

As there are no external loading applied at the side faces, the normal stress at every point on the side faces for each layer should be zero. However, this condition can not be satisfied exactly due to the assumptions in Eqs. (10) and (12). Instead, relaxed boundary conditions will be used by setting the integral or the average of the normal stress on side faces be zero. As stated before, the surface layer, which typically acts as a protective layer made by brittle metal oxide, is the layer that is easiest to be cracked. Therefore, in order to predict the fracture ERR or the maximum stress in the surface layer more accurately, the averaged normal stress at the side face of surface layer is used as one boundary condition while the integral of the normal stress across the side faces for all other layers is set to be zero to provide the other boundary condition as follows:

$$\int_0^{\lambda} \int_{t_{N-1}}^{h} \sigma_{xx}^N (x=\lambda) dz dy = 0 \tag{59}$$

and

$$\int_0^{\lambda} \sum_{i=1}^{N-1} \left[\int_{t_{i-1}}^{t_i} \sigma_{xx}^i (x=\lambda) dz \right] dy = 0 \tag{60}$$

This choice to combine lower-lying layers into the necessary second boundary condition is not unique and we do not know, a priori, what the best choice would be but we have performed numerical experiments comparing different versions of Eqs. (59) and (60) and found that the previous boundary conditions provide the best agreement with solutions found via finite-element analysis.

Substituting Eqs. (52) and (54) into Eqs. (59) and (60) yields

$$B_1 \sum_{i=1}^{N-1} K_{i1} + \varepsilon_u \sum_{i=1}^{N-1} K_{i2} - \Delta T \sum_{i=1}^{N-1} (\alpha_i K_{i2}) = 0 \tag{61}$$

and

$$B_N K_{N1} + \varepsilon_u K_{N2} - \Delta T \alpha_N K_{N2} = 0 \tag{62}$$

where

$$K_{i1} = \begin{cases} \dfrac{E^i}{\xi_i (1-\nu_i^2)} Q_i \left[\lambda \cosh(C\lambda) + \dfrac{\nu_i}{C} \sinh(C\lambda) \right], & i \in [1, N-1] \\ \dfrac{E^N}{\xi_N (1-\nu_N^2)} \sin(\xi_N C h_N) \left[\lambda \cosh(C\lambda) + \dfrac{\nu_N}{C} \sinh(C\lambda) \right], & i = N \end{cases} \tag{63}$$

$$Q_i = H_{i2} \sin(\xi_i C t_i) - H_{i2} \sin(\xi_i C t_{i-1}) - H_{i1} \cos(\xi_i C t_i) + H_{i1} \cos(\xi_i C t_{i-1}) \tag{64}$$

and

$$K_{i2} = \frac{E^i}{1-\nu_i} \lambda h_i, \quad i \in [1, N] \tag{65}$$

Combining Eqs. (61), (62), and (56), all unknowns can be determined as

$$B_1 = \Delta T \frac{K_{N2} \sum_{i=1}^{N-1} (\alpha_i K_{i2}) - \alpha_N K_{N2} \sum_{i=1}^{N-1} K_{i2}}{K_{N2} \sum_{i=1}^{N-1} K_{i1} - K_{N1} K \sum_{i=1}^{N-1} K_{i2}} \tag{66}$$

$$D_N = K B_1 \tag{67}$$

$$\varepsilon_u = \frac{\Delta T K_{N2} \alpha_N - B_1 K_{N1} K}{K_{N2}} \tag{68}$$

where

Downloaded from ascelibrary.org by Columbia University on 06/11/19. Copyright ASCE. For personal use only; all rights reserved.

$$K = \frac{H_{(N-1)1}\sin(\xi_{N-1}Ct_{N-1}) + H_{(N-1)2}\cos(\xi_{N-1}Ct_{N-1})}{\cos(\xi_N Ch_N)} \quad (69)$$

Numerical Verification of the General Solutions

In this section, the displacement and residual stress fields in the advanced polymeric solar reflectors, driven by a temperature change, are solved using the solutions developed in the section "Formulations for 3D Elastic Field Analysis." In order to verify the proposed model and investigate its applicability to multilayered structures with various geometries, the elastic field predicted by the theoretical model are compared with FE simulation results. In addition, some parametric studies of how layer thicknesses affect the solutions and their accuracies are conducted in this section.

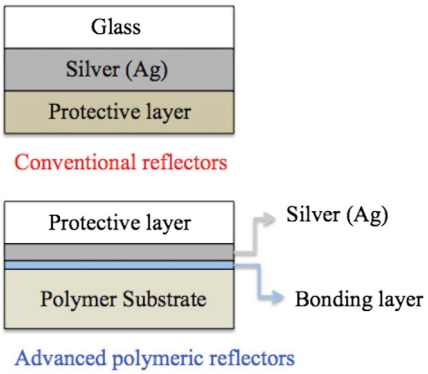

Fig. 2. Schematic reflector designs. (Data from Kennedy et al. 2005; Jorgensen et al. 2010; Zhang et al. 2016.)

Table 1. Material properties and geometric constants used in the FE model

Property	PET	Copper	Silver	Titania
Modulus (GPa)	$E^1 = 3.9$	$E^2 = 110$	$E^3 = 83$	$E^4 = 230$
Poisson ratio	$\nu_1 = 0.3$	$\nu_2 = 0.34$	$\nu_3 = 0.37$	$\nu_4 = 0.27$
Coefficient of thermal expansion (10^{-6}/°C)	$\alpha_1 = 59.4$	$\alpha_2 = 17$	$\alpha_3 = 18$	$\alpha_4 = 9$
Thickness (μm)	$h_1 = 180$	$h_2 = 0.01$	$h_3 = 0.1$	$h_4 = 0.2$
Length (μm)	—	2λ	4,000	—

Sources: Data from Zhang et al. (2016); ToolBox (2016).

Residual Stress in the Advanced Polymeric Solar Reflectors

As multilayered structures, advanced polymeric solar reflectors shown schematically in Fig. 2 have been widely applied in concentrated solar power systems (Kennedy et al. 2005; Jorgensen et al. 2010; Sutter et al. 2012; Sansom et al. 2016) due to their higher reflectance and lower cost for both manufacturing and installation compared with the traditional solar reflector design that utilizes silver pained on the back of glass (Fu et al. 2004; Kennedy et al. 2005; Park et al. 2011; Guo et al. 2014; Zhang et al. 2016).

These advanced polymeric reflectors are manufactured by depositing multiple thin metal and metal oxide layers on the polymer substrates, with the oxides used both to impart abrasion resistance (Kennedy et al. 2005; Jorgensen et al. 2010; Sansom et al. 2016) or to improve the reflectance through thin-film interference (Sutter et al. 2012). However, under a sufficiently large temperature change, the surface layers would suffer premature damage due to OMF, which would cause the loss both of protective functionality and of the reflectance efficiency. In order to understand the fracture mechanism, the displacement and residual stress fields in the surface layer of the advanced polymeric solar reflectors driven by a temperature change are first obtained by applying the proposed model in section "Formulations for 3d Elastic Field Analysis." Then FE simulations are conducted using the commercial software ABAQUS version 6.13 to verify the theoretical predictions. The material properties and geometric constants of the advanced polymeric solar reflector used in this FE analysis are taken from literature values (Zhang et al. 2016; ToolBox 2016) and are provided in Table 1. For our system, Layers 1, 2, 3, and 4 represent the polymer substrate [in this study taken to be polyethylene terephthalate (PET)], a thin bonding layer (copper), a silver layer, and a protective metal oxide layer (titania), respectively. The temperature change is set to be 40°C in this simulation.

Considering the symmetry, one-quarter of the structure is simulated as shown in Fig. 3(a), with symmetric boundary conditions applied at both the left side face and the front side face. The displacement along the thickness direction at the bottom is fixed and the interfaces between layers are tied together to avoid any debonding or slipping. Fig. 3(b) shows the mesh of the FE model in which 3D stress, eight-node linear brick elements are used to simulate the

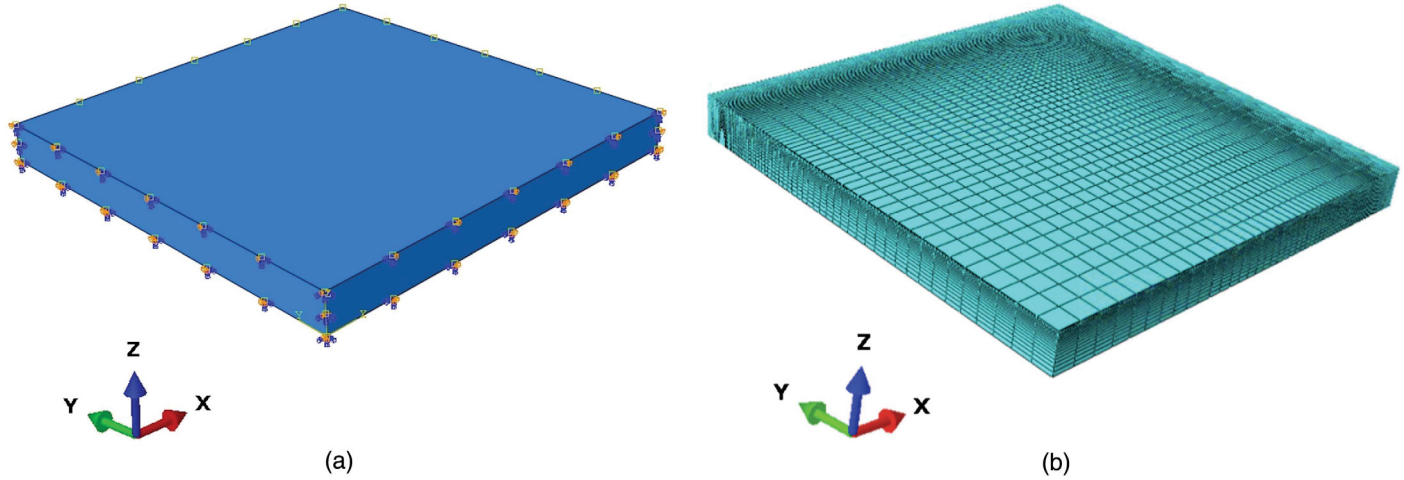

Fig. 3. FE simulation: (a) FE model and boundary conditions; and (b) mesh of the FE model.

Downloaded from ascelibrary.org by Columbia University on 06/11/19. Copyright ASCE. For personal use only; all rights reserved.

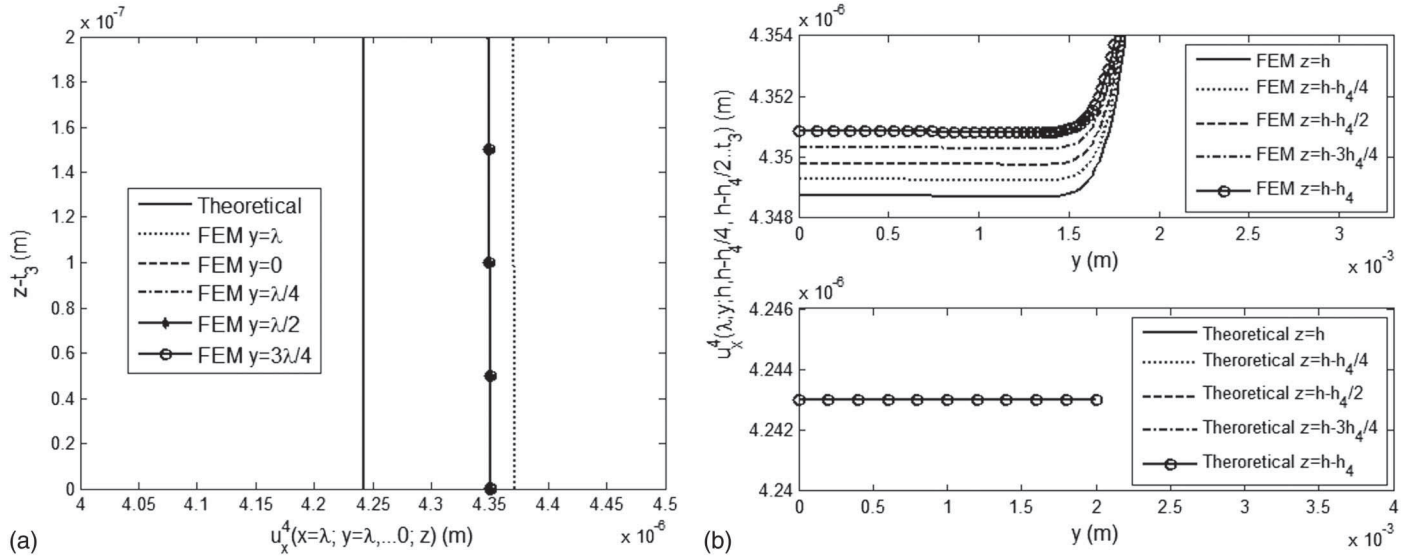

Fig. 4. Comparison between theoretical solutions and FE analysis results for u_x^4: (a) across thickness of surface layer at different y; and (b) along width direction at different depths.

materials. In order to improve the computational efficiency and accuracy, a gradient mesh is applied along the length, width, and thickness directions. From the plane of symmetry to the side faces, the mesh size increases from 0.002 to 0.1 mm. Four layers of elements with uniform thickness are used to mesh Layer 2, Layer 3, and Layer 4 while the thickness of elements in Layer 1 increases from 0.004 to 0.02 mm from the top to the bottom. In total, 131,061 elements are used for the whole model. A constant temperature field of 0°C is defined in the initial step, then modified to be 40°C in the following step to model the application of a temperature change of 40°C.

The distribution of u_x^4 across the thickness of surface layer with different y-coordinates is shown in Fig. 4(a). Because our derivation assumes u_x is independent of y-coordinates in Eq. (12), only one distribution of u_x^4 is obtained from the theoretical model for different y-coordinates. Both the theoretical solutions and the FE analysis results show that u_x^4 will decrease from the interface to the top surface because the thermal expansion coefficient of surface layer is smaller than that of the lower layers, therefore the lower layer would stretch the surface layer by applying a shearing stress at the interface and this shearing stress would decrease from the interface to the top surface. Although the FE analysis results show that u_x^4 will have minor changes with the change of y-coordinates, the theoretical model can still capture the distribution of u_x^4 across the thickness of the surface layer at different y-coordinates with a maximum difference smaller than 3%. The distribution of u_x^4 along the width direction at different depths is presented in Fig. 4(b), both theoretical solutions and FE analysis results show that u_x^4 would keep constant with the change of y approximately, which means our assumption in Eq. (12) is reasonable.

Fig. 5(a) presents the distribution of normal stress σ_{xx}^4. It shows that the plotted distributions of σ_{xx}^4 at different y are almost overlapped (these curves are enlarged and shown as the figure at the right side) when y is smaller than λ, while both the theoretical model (solid line marked with open circle at bottom in the main figure) and FE simulation (dash line marked with open circle at bottom) predict a much smaller σ_{xx}^4 at the edge, where $y = \lambda$. This indicates that the normal stress σ_{xx}^4 will not change significantly with respect to y except at the edge of the slab. Also, a good agreement between the theoretical predictions and the FE simulation results is observed as the maximum difference, which is reached at the edge where $y = \lambda$, is smaller than 3%. Fig. 5(b) presents the distribution of σ_{xx}^4 across the width, indicating that the normal stress would decrease from the center to the edge and the difference between the simulation results and the theoretical prediction is within 2%, which denotes the accuracy of our theoretical model.

In addition, the distribution of shear stress at the interface between titania and silver layers is presented in Fig. 6. It shows that the shear stress from both the present model and FE results gradually increases from the center toward the free end. From the present model, the shear stress, τ_{xz}, is independent of y. Similarly, the simulated shear stress does not vary substantially with respect to y-coordinates as all curves calculated from finite-element method (FEM) are almost overlapped. For the innermost area, away from the edges, the theoretically predicted shear stress agrees well with that from the FE simulation; however, a higher stress concentration is captured by the present model near the edge, while the free stress, which satisfies the free traction condition, was predicted by FEM. Overall, a good agreement between the theoretical solutions and FE simulation results is observed, demonstrating the accuracy of the developed model.

Parametric Studies

To investigate the effect of geometry, particularly the thickness of each layer, on the accuracy of the proposed model, we conducted some parametric studies. As shown in last section, the maximum difference between theoretical predictions and FE simulation results would be reached at the edge, therefore only the displacement and residual stress at the edge of the surface coating will be provided in this section.

The effect of h_2 on the distribution of displacement and residual stress at the corner of the surface layer is shown in Fig. 7. Based on Fig. 7(a), the theoretically predicted displacement would approach to the FE simulation results as h_2 increases. When h_2 is equal to h_1, the theoretical solutions would overlap with the FE simulation results. However, for the distribution of normal stress, the best agreement is gained when $h_2 = 1$ μm. As h_2 increases or decreases, the difference between the theoretical solutions and FE simulation

J. Eng. Mech., 2019, 145(3): 04019010

Downloaded from ascelibrary.org by Columbia University on 06/11/19. Copyright ASCE. For personal use only; all rights reserved.

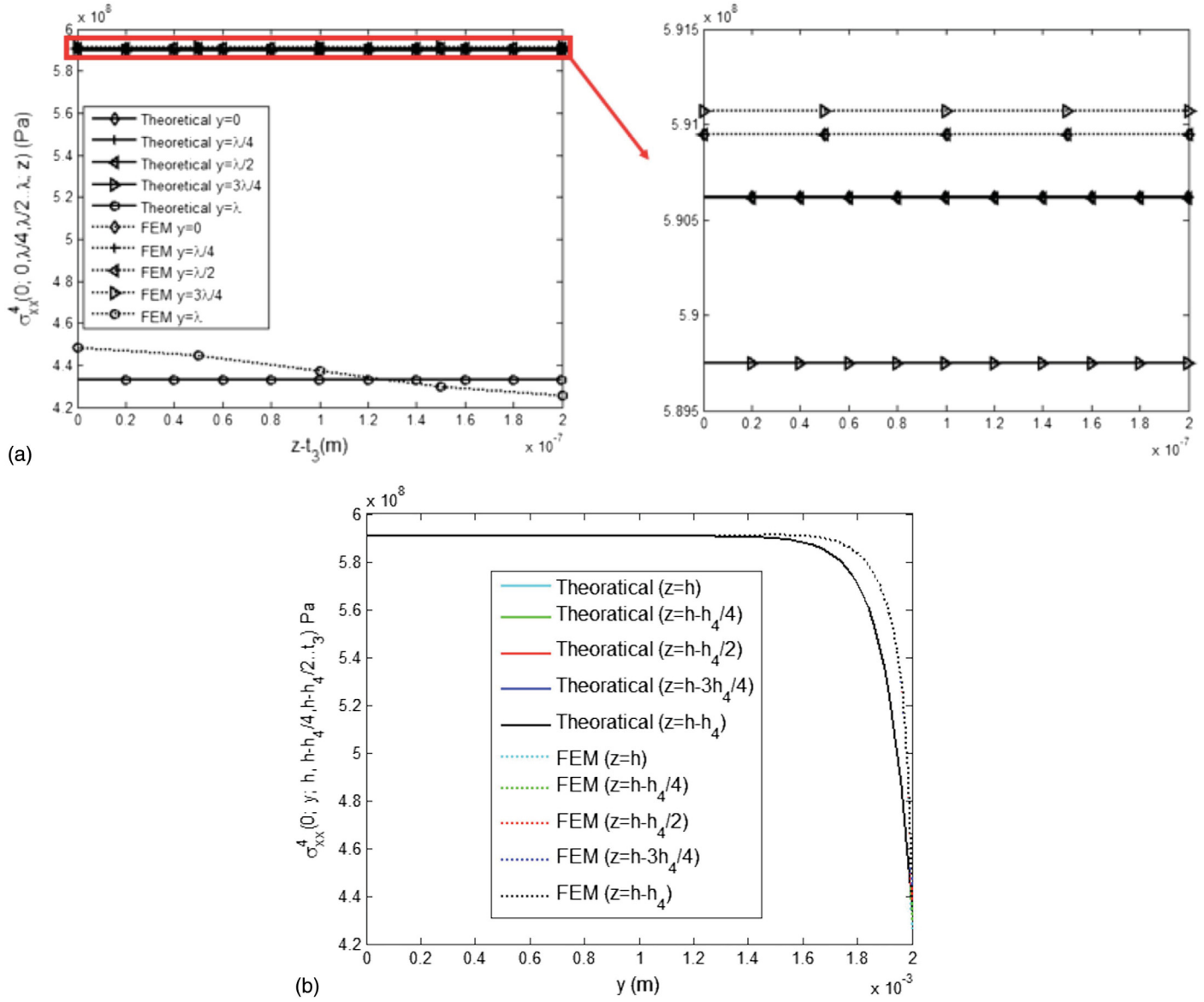

Fig. 5. Comparison between the theoretical solutions and the FE simulation results for normal stress σ_{xx}^4: (a) across thickness of surface layer at different y; and (b) along width direction at different depths.

results would increase. When $h_2 = h_1$, the maximum difference can become as large as 15%. The reason for the large deviation is that with the increase of h_2, the edge effect or the singularity in the solution at the corner becomes more and more significant. Fig. 8 shows the distribution of normal stress at locations far away from the edge ($y = 3\lambda/4$ and $y = \lambda/2$) for different h_2. It indicates that the theoretical model can predict a more-accurate stress distribution for the inner area: when $y = 3\lambda/4$, the maximum difference between the theoretical solution and FE simulation results is smaller than 5%.

Figs. 9 and 10 show the effect of changing layer thicknesses h_3 and h_4 on the accuracy of the model, respectively. Similar to what is found for h_2, our model can predict a more accurate displacement distribution with the increase of h_3 and h_4. The prediction of normal stress at the edge does get worse with the increase of h_3 or h_4 due to the increase of edge effect or singularity at the corner; however, at locations away from the edge, the theoretical solutions still agree well with the FE simulations results, which is similar as shown in Fig. 8.

Based on this parametric study, the presented model can predict the elastic distribution accurately in the surface layer of the multilayered structures with various thickness ratios when away from the edge. Although the difference between the theoretical predictions and FE simulation results is large at the edge due to edge effect or singularity, this error is expected to have a minor effect on the fracture analysis we conduct in the next section.

Fracture Analysis

Consider the section with OMFs at each side face in Fig. 1. When the temperature change reaches a critical value, a steady-state channeling straight crack will initiate at the middle edge of the section. There are two models for the fracture analysis, namely the strength model and energy model. The strength model is based on the maximum normal stress at which fracture would initiate when the maximum normal stress is higher than the strength (Ochiai et al. 2005).

J. Eng. Mech., 2019, 145(3): 04019010

Downloaded from ascelibrary.org by Columbia University on 06/11/19. Copyright ASCE. For personal use only; all rights reserved.

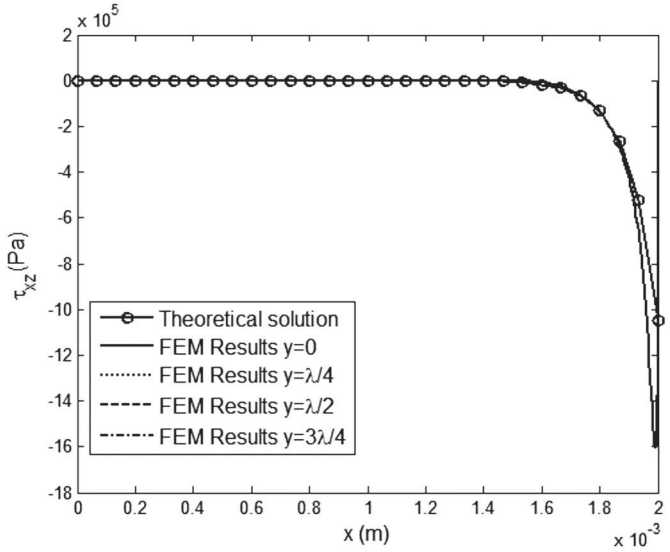

Fig. 6. Distribution of shear stress, τ_{xz}, at the interface between titania and silver layers.

According to the results shown in Fig. 5(b), the maximum normal stress is reached at the center, where ($y = 0$), and therefore the cracking pattern in the surface layer can be analyzed easily by comparing the normal stress at the center with the strength. The energy model is based on the fracture ERR during the process of cracking (Beuth 1992). To recover an OMF, the normal stress along the central line just before the fracture initiates needs to be applied along the cracking surface to recover the crack opening displacement. As after cracking, the section is broken into four pieces, and the displacement field in each quarter can also be solved by replacing λ with $\lambda/2$ in the new local coordinate system. Therefore, the crack opening displacement is solved. According to Beuth (1992), the fracture ERR in surface layer is equivalent with the work done to close the crack opening displacement and can be obtained from the integration

$$G = \frac{1}{\lambda h_4}\int_0^{\lambda}\int_{t_3}^{h}\sigma_{xx}^4(0,y,z)[u_x^4(\lambda,t_3) - u_x^4(\lambda,z)]dzdy \qquad (70)$$

By substituting the solved elastic field in section "Formulations for 3D Elastic Field Analysis" into Eq. (70), the fracture ERR in surface layer of the multilayered reflector system can be calculated. Note that the calculation of fracture ERR, which is used for fracture analysis based on an energy model (Beuth 1992), uses the *averaged* normal stress, whereas fracture analysis based on the strength model (DeGarmo et al. 1997) uses the maximum normal stress that is reached at $y = 0$ according to Fig. 5(b), so the inaccurate normal stress distribution at the edge may be expected to have a minor effect on the fracture analysis using either the strength or energy model.

Fig. 11 presents the change of fracture ERR with respect to crack spacing and surface layer thickness, where the horizontal lines indicates the critical fracture ERR. It shows that the fracture ERR would increase rapidly as the crack spacing increases until it reaches 4 mm. Beyond this point, the fracture ERR does not change any more although the crack spacing increases. Also, the critical fracture ERR will be reached at $\lambda = 0.8$ mm, indicating that under this temperature change ($\Delta T = 1{,}450$°C), the potential crack spacing of the given geometry ($h_1 = 0.18$ mm, $h_2 = 10$ nm, $h_3 = 100$ nm, $h_4 = 200$ nm) will be smaller than 0.8 mm. Fig. 11(b) shows the variance of the fracture ERR with respect to the surface layer's thickness with constant crack spacing $\lambda = 0.2$ mm under a temperature change of 310°C. The fracture ERR increases linearly with the surface layer's thickness increases until it reaches a maximum. After this point, the fracture ERR decreases as the thickness increases. In addition, the fracture ERR is higher than the critical value when 20 μm $< h_4 <$ 115 μm, which means fracture propagation can occur when h_4 is in this range.

Once the fracture ERR is obtained, energy model can be applied to conduct fracture analysis. The criterion used by the energy model is that new crack would nucleate once the fracture ERR reaches the critical fracture ERR as shown in Eq. (71)

$$G \geq G_{cr} \qquad (71)$$

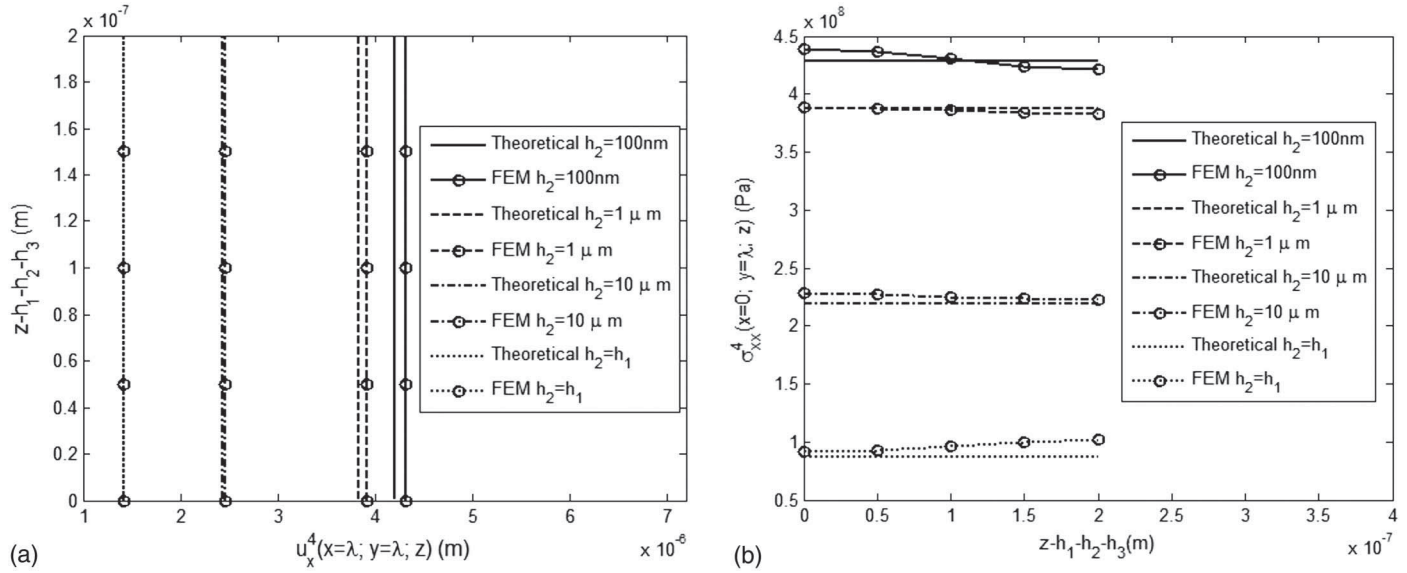

Fig. 7. Comparison between theoretical solutions and FE simulation results for different h_2: (a) for displacement $u_x^4(x = \lambda, y = \lambda, z)$; and (b) for normal stress $\sigma_{xx}^4(x = 0, y = \lambda, z)$.

Downloaded from ascelibrary.org by Columbia University on 06/11/19. Copyright ASCE. For personal use only; all rights reserved.

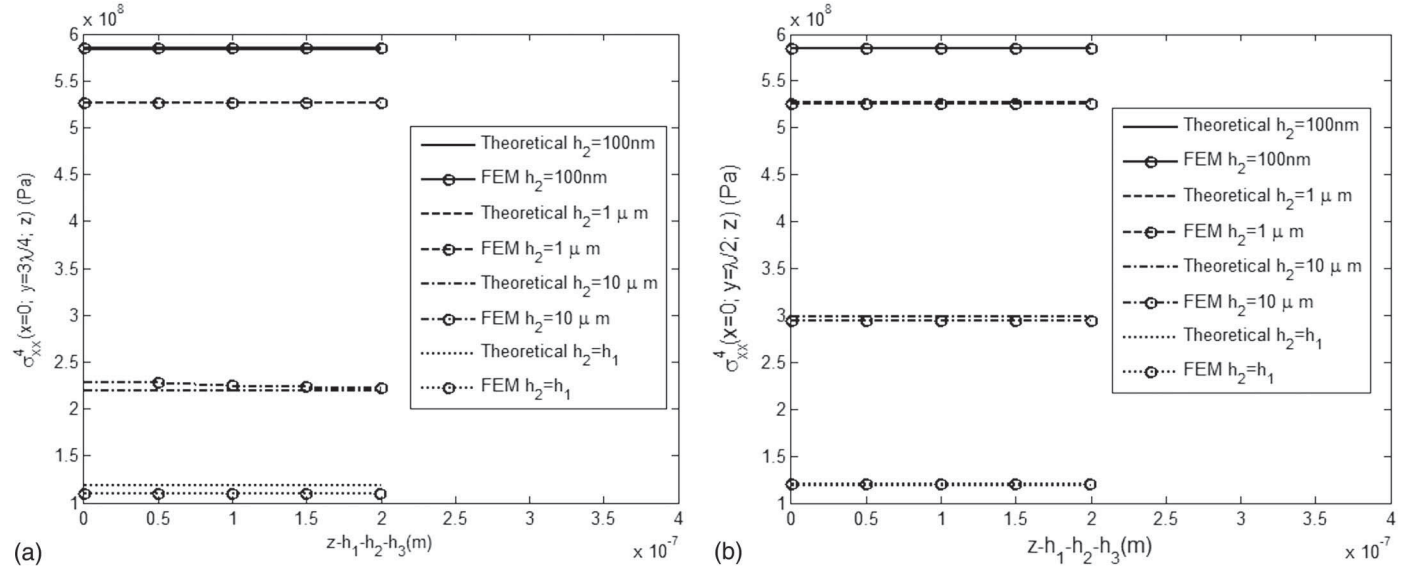

Fig. 8. Distribution of normal stress at inner area: (a) $y = 3\lambda/4$; and (b) $y = \lambda/2$.

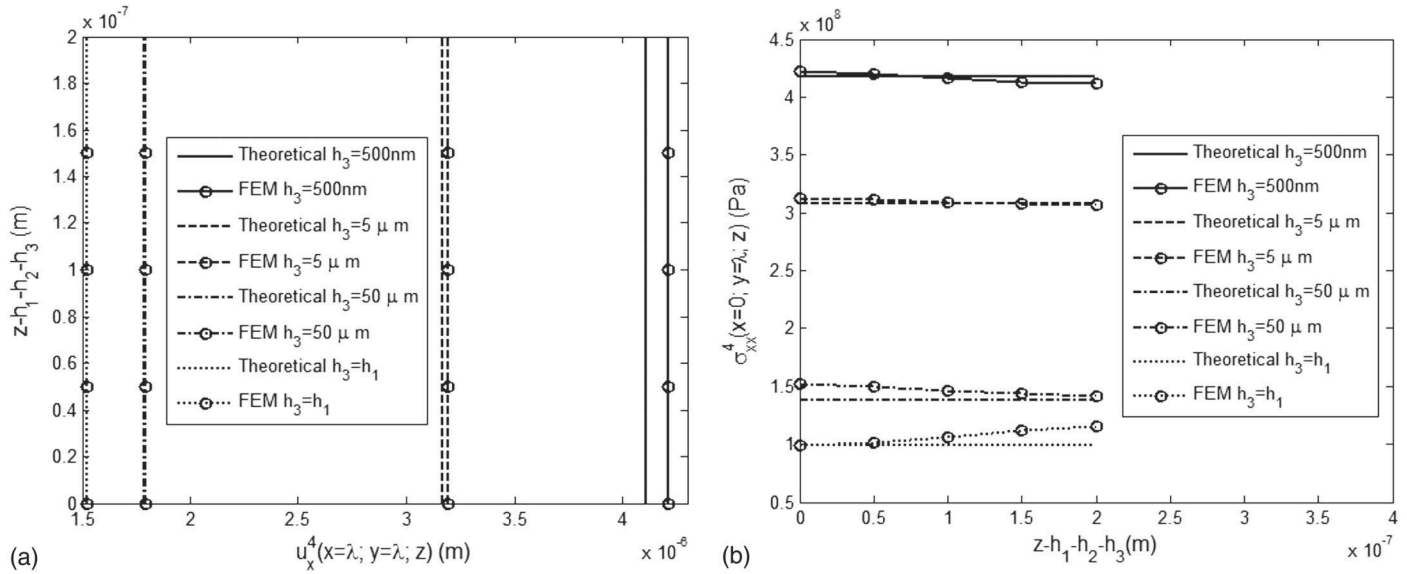

Fig. 9. Comparison between theoretical solutions and FE simulation results for different h_3: (a) for displacement $u_x^4(x = \lambda, y = \lambda, z)$; and (b) for normal stress $\sigma_{xx}^4(x = 0, y = \lambda, z)$.

where G_{cr} = critical fracture ERR of the surface layer. The G_{cr} of a thin coating layer is hard to measure using classic fracture tests, such as the four-point bending test (Askarinejad et al. 2016). By fitting the theoretically predicted crack pattern to the observed crack pattern in the protective metal oxide layer (titania) of an advanced polymeric solar reflector under uniaxial tension, Zhang et al. (2016) determined it as 0.277 N/m. Using the criterion as shown in Eq. (71) with this value of G_{cr}, the required temperature change to initiate new cracks in the surface layer with different geometries can be obtained and presented in Fig. 12. Based on Fig. 12(a), the required temperature change to create new cracks increases as the crack spacing decreases. When λ approaches 0.4 mm, the temperature change turns to infinity, which means no new fractures will infill and the fracture saturation has been reached. For this specified case ($h_1 = 0.18$ mm, $h_2 = 10$ nm, $h_3 = 100$ nm, $h_4 = 200$ nm), the saturated crack spacing can be approximately evaluated as 0.4 mm. Fig. 12(b) shows the variation of the required temperature change with respect to the surface layer's thickness at a constant crack spacing ($\lambda = 0.2$ mm) and indicates that the required temperature change to initiate a new crack in the surface layer will reduce as the surface coating thickness decreases until a critical thickness $h_{4_{cr}}$ is reached. Below this critical thickness, the required temperature change to crack the surface layer increases to be infinite and the fracture saturation would be reached. For this study, the critical thickness is about 2 μm for a crack length of 0.2 mm.

Summary and Conclusions

In this paper, a 3D elastic model has been presented to study the residual stress and predict OMF in multilayered structures, consisting of arbitrary layers, under thermal loading. By employing a

Downloaded from ascelibrary.org by Columbia University on 06/11/19. Copyright ASCE. For personal use only; all rights reserved.

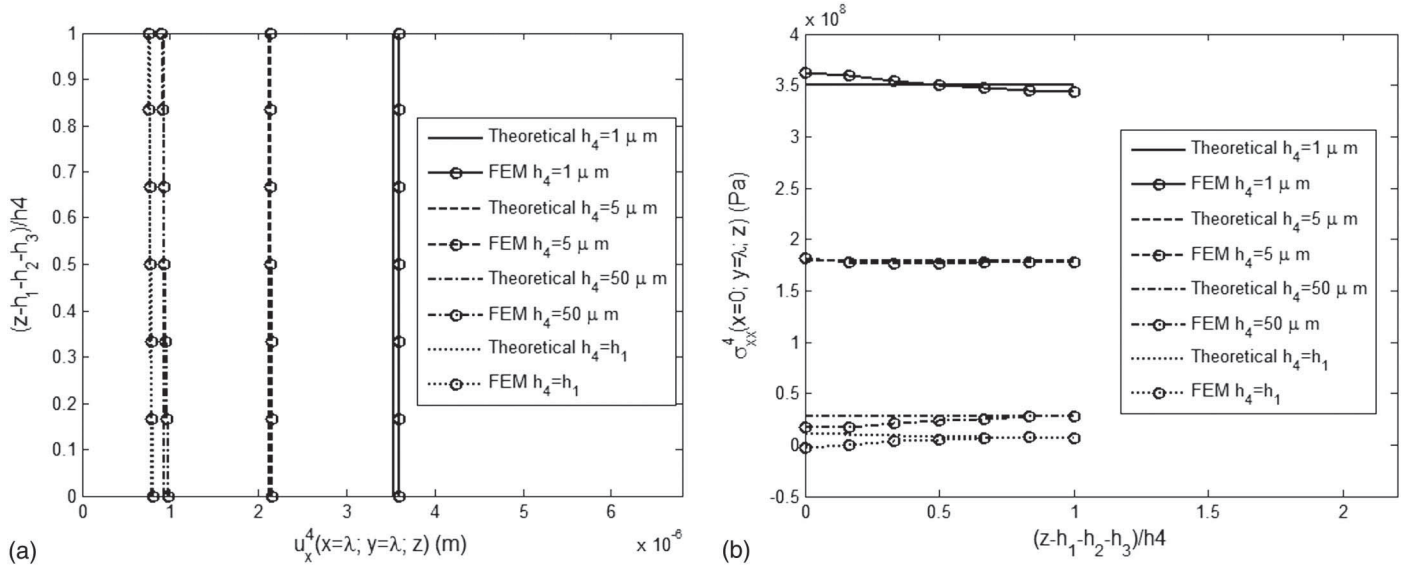

Fig. 10. Comparison between theoretical solutions and FE simulation results for different h_4: (a) for displacement $u_x^4(x = \lambda, y = \lambda, z)$; and (b) for normal stress $\sigma_{xx}^4(x = 0, y = \lambda, z)$.

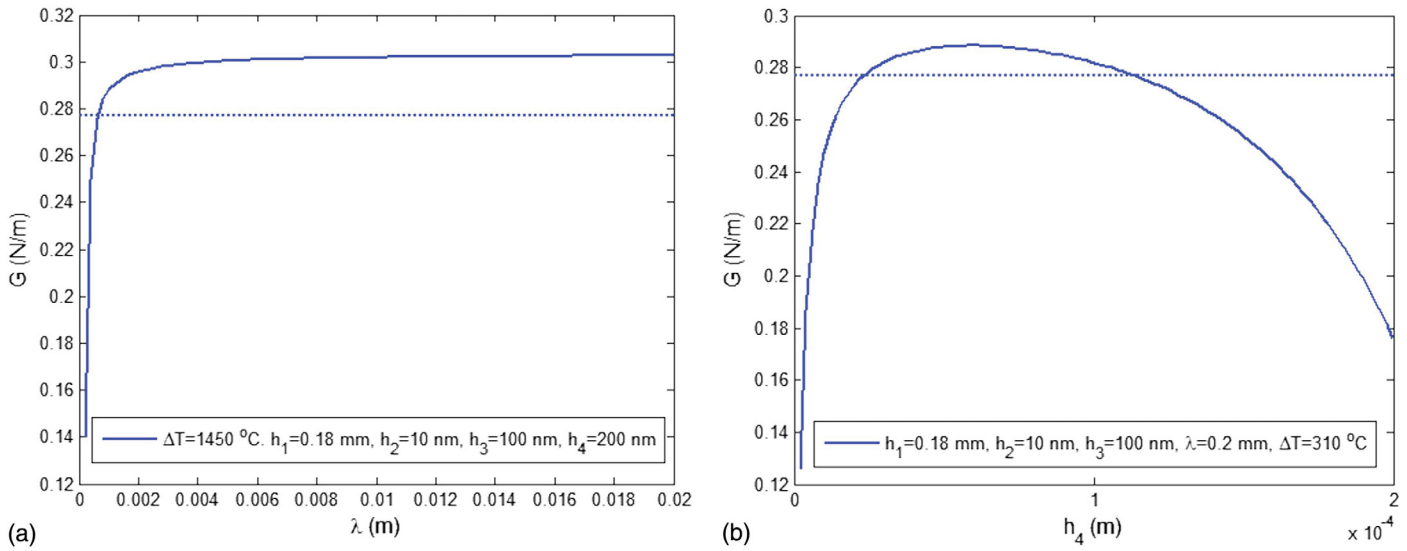

Fig. 11. Variance of ERR with respect to (a) crack spacing for a particular set of thickness indicated in the figure; and (b) surface layer's thickness at fixed crack spacing.

nonshearing assumption and the assumption of free normal stress in thickness direction, the explicit solution of displacement and stress was obtained through solving the elastic boundary value problem. In order to verify the proposed model, the elastic field in the advanced polymeric solar reflector were solved and compared with FE simulation results. The good agreement between the theoretical predictions and FE simulation results demonstrated the accuracy of the presented model. In addition, the effect of the geometry, particularly the thickness of each layer, on the accuracy of the theoretical model was investigated by the parametric study.

The results showed that the model could predict the displacement and stress fields in the inner area of multilayered structures with various thickness ratio between each layer accurately, although large difference between the theoretically predicted normal stress and FE simulated normal stress would be observed at the area very close to the edge due to the edge effect or singularity at the corner.

Based on the elastic solutions, the fracture ERR in the surface layer was calculated and used to study the fracture infilling and saturation. The results showed the following:

- The fracture ERR would increase rapidly as the crack spacing increased until a plateau stage was reached when the crack spacing approached 4 mm. Also, under the temperature change of 1,450°C, the potential crack spacing was smaller than 0.8 mm.
- With constant crack spacing, the fracture ERR approximately increased linearly with the surface coating thickness until it reached the convex point, at which the fracture saturation was reached. In this case ($\Delta T = 40$°C, $\lambda = 0.2$ mm, $h_1 = 0.18$ mm,

Downloaded from ascelibrary.org by Columbia University on 06/11/19. Copyright ASCE. For personal use only; all rights reserved.

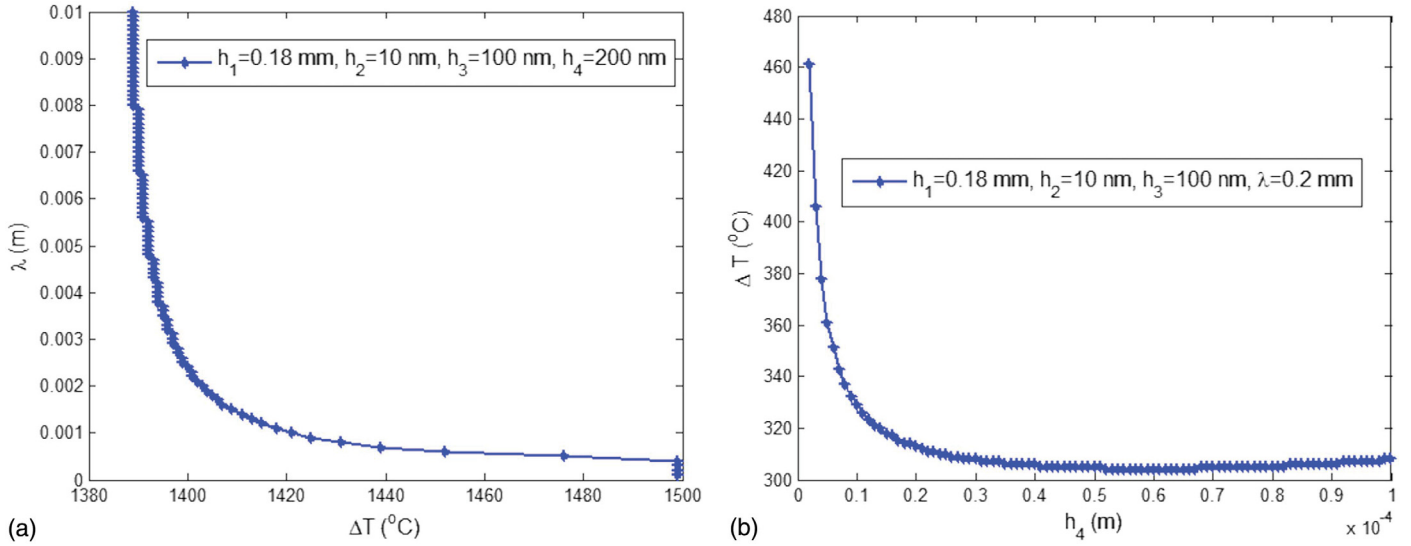

Fig. 12. Crack spacing development with respect to temperature change: (a) h_4 = constant; and (b) λ = constant.

$h_2 = 10$ nm, $h_3 = 100$ nm), fracture can propagate when the critical surface coating thickness is in the range of 20–115 μm.

- When the surface layer's thickness remained constant, the temperature change required to form a new crack would increase as the crack spacing decreased and fracture saturation would be reached when the crack spacing approached 0.4 mm.
- When the crack spacing was constant, the required temperature change to form a new crack would decrease as the surface layer's thickness decreased, until a critical surface coating thickness was reached. Under this critical thickness the required temperature change would increase to be infinite, which means the fracture saturation was obtained. For the crack spacing of 0.2 mm, the critical surface coating thickness was about 2 μm.

Overall, the presented model was able to capture the displacement and stress distributions in the multilayered structures accurately and predict the fracture initiation, infilling, and saturation of the surface layer successfully. Compared with the previous 2D models and simplified 3D models presented in the introduction part, this model included the effects of material properties and geometry constants of each layer on the displacement and stress distributions. Therefore, it could predict the fracture behavior more accurately. In addition, this presented model provided a general solution that could be used to analyze the stress distribution and fracture behavior of multilayered structures consisting of arbitrary layers.

Acknowledgments

This study was supported by the US Department of Energy under Contract No. DE-AC36-08-GO28308 with the National Renewable Energy Laboratory through the DOE SETP program and the US National Science Foundation under award No. 1738802 with the Center for Energy Harvesting Materials and Systems through NSF Industry/University Cooperative Research Center Program. The US Government retains, and the publisher, by accepting the article for publication, acknowledges that the US Government retains a nonexclusive, paid-up, irrevocable, worldwide license to publish or reproduce the published form of this study, or allow others to do so, for US Government purposes.

References

Ahmed, F., K. Bayerlein, S. Rosiwal, M. Göken, and K. Durst. 2011. "Stress evolution and cracking of crystalline diamond thin films on ductile titanium substrate: Analysis by micro-Raman spectroscopy and analytical modelling." *Acta Mater.* 59 (14): 5422–5433. https://doi.org/10.1016/j.actamat.2011.05.015.

Askarinejad, S., P. Kotowski, S. Youssefian, and N. Rahbar. 2016. "Fracture and mixed-mode resistance curve behavior of bamboo." *Mech. Res. Commun.* 78 (12): 79–85. https://doi.org/10.1016/j.mechrescom.2016.02.001.

Bai, T., and D. D. Pollard. 2000. "Spacing of fractures in a multilayer at fracture saturation." *Int. J. Fract.* 100 (4): 23–28. https://doi.org/10.1023/A:1018748026019.

Bai, T., D. D. Pollard, and H. Gao. 2000a. "Explanation for fracture spacing in layered materials." *Nature* 403 (6771): 753–756. https://doi.org/10.1038/35001550.

Bai, T., D. D. Pollard, and M. R. Gross. 2000b. "Mechanical prediction of fracture aperture in layered rocks." *J. Geophys. Res. Solid Earth* 105 (B1): 707–721. https://doi.org/10.1029/1999JB900303.

Berry, B. 1989. "Anelastic relaxation and diffusion in thin-layer materials." In *Diffusion phenomena in thin films and microelectronic materials*, 73–145. Yorktown Heights, NY : Noyes Data Corporation.

Beuth, J. 1992. "Cracking of thin bonded films in residual tension." *Int. J. Solids Struct.* 29 (13): 1657–1675. https://doi.org/10.1016/0020-7683(92)90015-L.

Beuth, J., and N. Klingbeil. 1996. "Cracking of thin films bonded to elastic-plastic substrates." *J. Mech. Phys. Solids* 44 (9): 1411–1428. https://doi.org/10.1016/0022-5096(96)00042-7.

Chai, H. 2011. "Channel cracking in inelastic film/substrate systems." *Int. J. Solids Struct.* 48 (7): 1092–1100. https://doi.org/10.1016/j.ijsolstr.2010.12.014.

Chai, H., and J. Fox. 2012. "On delamination growth from channel cracks in thin-film coatings." *Int. J. Solids Struct.* 49 (22): 3142–3147. https://doi.org/10.1016/j.ijsolstr.2012.06.012.

Chen, F., X. He, P. Prieto-Munoz, and H. Yin. 2015. "Opening-mode fractures of a brittle coating bonded to an elasto-plastic substrate." *Int. J. Plast.* 67 (4): 171–191. https://doi.org/10.1016/j.ijplas.2014.10.007.

Çolak, A. 2001. "Parametric study of factors affecting the pull-out strength of steel rods bonded into precast concrete panels." *Int. J. Adhes. Adhes.* 21 (6): 487–493. https://doi.org/10.1016/S0143-7496(01)00028-8.

DeGarmo, E. P., J. T. Black, R. A. Kohser, and B. E. Klamecki. 1997. *Materials and process in manufacturing*. London: Prentice Hall.

Downloaded from ascelibrary.org by Columbia University on 06/11/19. Copyright ASCE. For personal use only; all rights reserved.

Evans, A., and J. Hutchinson. 1995. "The thermomechanical integrity of thin films and multilayers." *Acta Metall. Mater.* 43 (7): 2507–2530. https://doi.org/10.1016/0956-7151(94)00444-M.

Freund, L. B., and S. Suresh. 2004. *Thin film materials: Stress, defect formation and surface evolution*. Cambridge, UK: Cambridge University Press.

Fu, Y., H. Du, W. Huang, S. Zhang, and M. Hu. 2004. "TiNi-based thin films in MEMS applications: A review." *Sens. Actuators, A* 112 (2–3): 395–408. https://doi.org/10.1016/j.sna.2004.02.019.

Guo, C. F., T. Sun, Q. Liu, Z. Suo, and Z. Ren. 2014. "Highly stretchable and transparent nanomesh electrodes made by grain boundary lithography." *Nat. Commun.* 5: 3121. https://doi.org/10.1038/ncomms4121.

He, X., F. Chen, and H. Yin. 2017. "Opening-mode micro-cracking in brittle coatings on ductile wires/rods." *Int. J. Damage Mech.* 26 (1): 119–146. https://doi.org/10.1177/1056789516659330.

Hsueh, C., and M. Yanaka. 2003. "Multiple film cracking in film/substrate systems with residual stresses and unidirectional loading." *J. Mater. Sci.* 38 (8): 1809–1817. https://doi.org/10.1023/A:1023200415364.

Hutchinson, J. W. 1996. *Stresses and failure modes in thin films and multilayers*. Notes for a Dcamm Course. Lyngby, Denmark: Technical Univ. of Denmark.

Jorgensen, G., R. Gee, and M. DiGrazia. 2010. *Development and testing of abrasion resistant hard coats for polymer film reflectors*. NREL/CP-5500-49273. Golden, CO: National Renewable Energy Libratory.

Kennedy, C., K. Terwilliger, and M. Milbourne. 2005. *Development and testing of solar reflectors*. NREL/CP-520-36582. Golden, CO: National Renewable Energy Libratory.

Li, J., and T.-W. Chou. 1997. "Elastic field of a thin-film/substrate system under an axisymmetric loading." *Int. J. Solids Struct.* 34 (35–36): 4463–4478. https://doi.org/10.1016/S0020-7683(97)00053-X.

Ochiai, S., H. Okuda, S. Iwamoto, T. Tomida, T. Nakamura, M. Tanaka, and M. Hojo. 2005. "Multiple-cracking phenomenon of the galvannealed coating layer on steels under thermal and tensile stresses." *Metall. Mater. Trans. A* 36 (7): 1807–1816. https://doi.org/10.1007/s11661-005-0044-0.

Ohring, M. 2001. *Materials science of thin films*. Hoboken, NJ: Academic Press.

Park, J. S., H. Chae, H. K. Chung, and S. I. Lee. 2011. "Thin film encapsulation for flexible AM-OLED: A review." *Semicond. Sci. Technol.* 26 (3): 034001.

Roy, U., and C. Ghosh. 2016. "Residual stress analysis in galvannealed coating." *Ironmaking Steelmaking* 43 (6): 465–472. https://doi.org/10.1080/03019233.2016.1142055.

Sansom, C., A. Fernández-García, F. Sutter, H. Almond, P. King, and L. Martnez-Arcos. 2016. "Soiling and cleaning of polymer film solar reflectors." *Energies* 9 (12): 1006. https://doi.org/10.3390/en9121006.

Schwarzer, N., and F. Richter. 2006. "On the determination of film stress from substrate bending: Stoney's formula and its limits." Accessed April 1, 2018. https://monarch.qucosa.de/api/qucosa%3A18453/attachment/ATT-0/.

Stoney, G. G. 1909. "The tension of metallic films deposited by electrolysis." *Proc. R. Soc. London, Ser. A* 82 (553): 172–175. https://doi.org/10.1098/rspa.1909.0021.

Suo, Z., and J. W. Hutchinson. 1989. "Steady-state cracking in brittle substrates beneath adherent films." *Int. J. Solids Struct.* 25 (11): 1337–1353. https://doi.org/10.1016/0020-7683(89)90096-6.

Sutter, F., S. Ziegler, M. Schmücker, P. Heller, and R. Pitz-Paal. 2012. "Modelling of optical durability of enhanced aluminum solar reflectors." *Sol. Energy Mater. Sol. Cells* 107 (11): 37–45. https://doi.org/10.1016/j.solmat.2012.07.027.

Thouless, M., Z. Li, N. Douville, and S. Takayama. 2011. "Periodic cracking of films supported on compliant substrates." *J. Mech. Phys. Solids* 59 (9): 1927–1937. https://doi.org/10.1016/j.jmps.2011.04.009.

Timm, D., B. Guzina, and V. Voller. 2003. "Prediction of thermal crack spacing." *Int. J. Solids Struct.* 40 (1): 125–142. https://doi.org/10.1016/S0020-7683(02)00496-1.

ToolBox. 2016. "The engineering toolbox." Accessed April 1, 2018. https://www.engineeringtoolbox.com/.

Wellner, P., O. Kraft, G. Dehm, J. Andersons, and E. Arzt. 2004. "Channel cracking of β-NiAl thin films on Si substrates." *Acta Mater.* 52 (8): 2325–2336. https://doi.org/10.1016/j.actamat.2004.01.023.

Xia, Z. C., and J. W. Hutchinson. 2000. "Crack patterns in thin films." *J. Mech. Phys. Solids* 48 (6): 1107–1131. https://doi.org/10.1016/S0022-5096(99)00081-2.

Ye, T., Z. Suo, and A. Evans. 1992. "Thin film cracking and the roles of substrate and interface." *Int. J. Solids Struct.* 29 (21): 2639–2648. https://doi.org/10.1016/0020-7683(92)90227-K.

Yin, H. M. 2010a. "Fracture saturation and critical thickness in layered materials." *Int. J. Solids Struct.* 47 (7): 1007–1015. https://doi.org/10.1016/j.ijsolstr.2009.12.016.

Yin, H. M. 2010b. "Opening-mode cracking in asphalt pavements: Crack initiation and saturation." *Road Mater. Pavement Des.* 11 (2): 435–457. https://doi.org/10.1080/14680629.2010.9690283.

Yin, H. M., W. Buttlar, and G. H. Paulino. 2007a. "Simplified solution for periodic thermal discontinuities in asphalt overlays bonded to rigid pavements." *J. Transp. Eng.* 133 (1): 39–46. https://doi.org/10.1061/(ASCE)0733-947X(2007)133:1(39).

Yin, H. M., G. Paulino, and W. Buttlar. 2008. "An explicit elastic solution for a brittle film with periodic cracks." *Int. J. Fract.* 153 (1): 39–52. https://doi.org/10.1007/s10704-008-9286-3.

Yin, H. M., G. Paulino, W. Buttlar, and L. Sun. 2007c. "Micromechanics-based thermoelastic model for functionally graded particulate materials with particle interactions." *J. Mech. Phys. Solids* 55 (1): 132–160. https://doi.org/10.1016/j.jmps.2006.05.002.

Yin, H. M., and P. A. Prieto-Muñoz. 2013. "Stress transfer through fully bonded interface of layered materials." *Mech. Mater.* 62: 69–79. https://doi.org/10.1016/j.mechmat.2013.03.007.

Zhang, C., F. Chen, M. H. Gray, R. Tirawat, and R. E. Larsen. 2017. "An elasto-plastic solution for channel cracking of brittle coating on polymer substrate." *Int. J. Solids Struct.* 120 (11): 125–136. https://doi.org/10.1016/j.ijsolstr.2017.04.033.

Zhang, C., M. H. Gray, R. Tirawat, R. E. Larsen, and F. Chen. 2016. *Effects of UV aging on the cracking of titanium oxide layer on poly (ethylene terephthalate) substrate*. NREL/CP-2C00-65867. Golden, CO: National Renewable Energy Laboratory.

Zhang, X., Y. Wu, B. Xu, and H. Wang. 2007. "Residual stresses in coating-based systems. Part I: Mechanisms and analytical modeling." *Front. Mech. Eng. China* 2 (1): 1–12. https://doi.org/10.1007/s11465-007-0001-2.

Downloaded from ascelibrary.org by Columbia University on 06/11/19. Copyright ASCE. For personal use only; all rights reserved.